# Crystal habit-directed gold deposition on pyrite: Surface chemical interpretation of the pyrite morphology indicative of gold enrichment

**Article** *in* Geochimica et Cosmochimica Acta · August 2019

DOI: 10.1016/j.gca.2019.08.011

CITATIONS
0

READS
307

**10 authors**, including:

Haiyang Xian
Chinese Academy of Sciences
**22** PUBLICATIONS **110** CITATIONS
SEE PROFILE

Hongping He
Chinese Academy of Sciences
**297** PUBLICATIONS **9,191** CITATIONS
SEE PROFILE

Jian-xi Zhu
Chinese Academy of Sciences
**226** PUBLICATIONS **5,832** CITATIONS
SEE PROFILE

Du Runxiang
Chinese Academy of Sciences
**3** PUBLICATIONS **7** CITATIONS
SEE PROFILE

Available online at www.sciencedirect.com

ScienceDirect

Geochimica et Cosmochimica Acta 264 (2019) 191–204

Geochimica et Cosmochimica Acta

www.elsevier.com/locate/gca

# Crystal habit-directed gold deposition on pyrite: Surface chemical interpretation of the pyrite morphology indicative of gold enrichment

Haiyang Xian [a], Hongping He [a,b,*], Jianxi Zhu [a], Runxiang Du [a,b], Xiao Wu [a,b] Hongmei Tang [a,b], Wei Tan [a], Xiaoliang Liang [a], Runliang Zhu [a], H. Henry Teng [c]

[a] *CAS Key Laboratory of Mineralogy and Metallogeny/Guangdong Provincial Key Laboratory of Mineral Physics and Materials, Guangzhou Institute of Geochemistry, Chinese Academy of Sciences (CAS), Guangzhou 510640, China*

[b] *University of Chinese Academy of Sciences, Beijing 100049, China*

[c] *Institute of Surface-Earth System Science, Tianjin University, Tianjin 300072, China*

Received 15 April 2019; accepted in revised form 8 August 2019; Available online 28 August 2019

**Abstract**

The occurrence of the {2 1 0} shape of pyrite crystals has been used as an empirical indicator for gold enrichment in ore deposits. Such indicating, also called 'typomorphism' in ore mineralogy, was conventionally attributed to environmental factors such as sulfur fugacity and temperature and pressure conditions in the ore-forming hydrothermal fluid. Here we show that the crystal-face specific redox reactivity of pyrite is also an important governing potency that drives gold enrichment in the pyrite crystals with particular shapes. This conclusion was drawn from data compiled from chemical analysis of field samples, laboratory testing of gold deposition on natural pyrite crystals, as well as theoretical calculations. Kinetic measurements of gold reductive deposition first revealed the highest precipitation rate on the {2 1 0} faces, particularly when pyrite crystals are enclosed by complex *forms* containing {2 1 0}. Corroborating with the experimental observations, density functional theory (DFT) calculations further indicated that the {2 1 0} possesses a high adsorption energy for gold, a high energy state of the highest occupied molecular orbital and consequently a low Eh. These results afford evidence supporting the view that the face specific reactivity, an intrinsic property of crystal, plays an important role in the gold concentration in pyrite and the occurrence of specific pyrite shapes. Our findings not only provide a surface chemical view for understanding the empirical prospecting method but also exemplified the significance of crystal face specific-reactivity in understanding crystallographic orientation related geochemical processes. The crystal face specific reactivity may be a critical factor controlling geochemical reactions at mineral-water interface, such as prebiotic synthesis on pyrite surfaces and mineral-water interface controlled kinetic isotope fractionation.



*Keywords:* Gold-bearing pyrite; Surface electronic structure; Surface reactivity; Pyrite face specific gold enrichment; Gold deposition

## 1. INTRODUCTION

Gold has been a measure of wealth for human society even since the metal's discovery in the early stage of civilization. As such, gold prospecting and exploration have never lost its frontier position in geoscience. Gold commonly occurs in sulfide minerals, such as bornite, chalcopyrite,

* Corresponding author at: CAS Key Laboratory of Mineralogy and Metallogeny/Guangdong Provincial Key Laboratory of Mineral Physics and Materials, Guangzhou Institute of Geochemistry, Chinese Academy of Sciences (CAS), Guangzhou 510640, China.

*E-mail address:* hehp@gig.ac.cn (H. He).

https://doi.org/10.1016/j.gca.2019.08.011

0016-7037/

as an "invisible" form in various ore deposits (Cook and Chryssoulis, 1990; Maddox et al., 1998; Cabri et al., 2000), including Carlin-type Au deposits (Palenik et al., 2004) and Archean Au lodes (Yang and Zhou, 2001; Goldfarb et al., 2005). Of these metal sulfides, pyrite is the most significant due to the indicative of crystal morphology to the enrichment of gold in ore deposits (Chen et al., 1987; Sazonov et al., 2009; Xue et al., 2014; Pshenichkin et al., 2015). For instance, high-concentration gold is emperically found to be correlatable to the occurrence of pyritohedral {2 1 0} and complex *form* of pyrite crystals (Table S1 in Supplementary Information). Although most of the collected data compiled in Table S1 are qualitative description, quantitative data from five gold deposits in China can be linearly plotted in Fig. 1.

The correlation in Fig. 1 could be interpreted by the occurrence of non-equilibrium {2 1 0} *form*, which is also linked to crystal size, i.e., specific surface area (SSA). Thus, the gold enrichment in pyritic {2 1 0} was traditionally attributed to SSA. Although the SSA dependence was frequently shown in both experimental and natural pyrites (Tauson et al., 2014; Tauson et al., 2018), conflicting observations were frequently reported in the literature. For instance, euhedral – subhedral pyrite pyritohedron (i.e., the {2 1 0} *form*) with larger crystal size (3–5 mm), from gold deposits of Beishan area in eastern Xinjiang, China, contain higher gold concentration (110 ppm) than that (3.33 pm) from euhedral {1 0 0} with small crystal size (1.5–3 mm) (Sun and He, 1997), indicating that the relation shown in Fig. 1 may have underlying controlling factors other than SSA only.

Alternately, the indicating of gold concentration by the crystal shape of pyrite (which is usually called 'typomorphic *forms*' in ore mineralogy) could also be interpreted indirectly as an indication of gold enrichment in high sulfur fugacity conditions. This interpretation was drawn based on that the development of pyritohedral morphology on pyrite crystals was shown to correlate with high S content in gold-bearing fluid at a wide pressure–temperature range (Chen et al., 1987; Cai and Zhou, 1994). An implicit hypothesis of this interpretation is that the partition of gold between pyrite and ore-forming fluid is irrelevant to the crystal faces and pertinent surface structures on pyrite grains. However, experimental studies provided direct evidence showing no correlation between gold's incorporation rate in pyrite and the solution phase concentration of gold ions (Mycroft et al., 1995). Furthermore, a plethora of literature data suggest that the reactivity of pyrite is crystallographic-direction specific (Guevremont et al., 1998; Elsetinow et al., 2000; Zhu et al., 2018). For instance, the oxidation rates of the {2 1 0} and {1 1 1} faces on pyrite are two orders of magnitude greater than that of the {1 0 0} face (Zhu et al., 2018). Hence, a critical gap exists in our current understanding of gold ore formation: is Au enrichment on specific pyrite faces associated with S-induced development of the {2 1 0} *form* or caused by the high surface reactivity of the {2 1 0} faces?

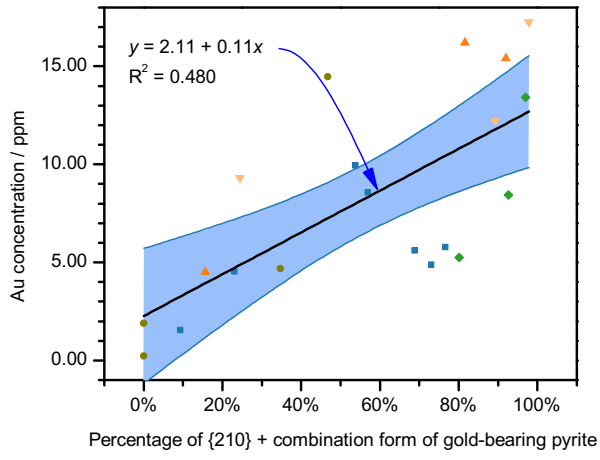


Fig. 1. Correlation between the occurrence of pyritohedral and complex pyrite crystals (%) and the gold concentration (ppm). Shaded area is 95% confidence interval for the linear correlation. ■ denotes data from Denggezhuang gold deposite (Xue et al., 2014); ● denotes data from Daiwangshan gold deposit in inner Mongolia (Wang et al., 2017); ▲ and ▼ denote data from Qixia gold deposit, and Xiadian gold deposit in Linglong, Shandong, respectively (Chen, 1987); ◆ denotes data from an anonymous gold deposit in Shandong, China (Yang and Huang, 1997).)

Whereas the adsorption and reductive precipitation of gold on pyrite surfaces is widely known (Mycroft et al., 1995; Widler and Seward, 2002), the fundamental driving factor responsible for $Au^{+}$ or $Au^{3+}$ to $Au^{0}$ transformation on specifically shaped pyrite crystals has not been elucidated in the context of physiochemical principles. For example, Hyland and Bancroft (1989) and Mycroft et al. (1995) examined gold precipitation on powdered pyrite using X-ray photoelectron spectroscopy and found that the mineral surfaces can serve as Au reducing agent. Mycroft et al. (1995) reported microphotographic evidence of gold aggregation from nano-particles to micro-grains on pyrite surface reacted in $AuCl_4^-$ solution. Recent data by Fu et al. (2017) revealed adsorption of gold nanoparticles with diameters of 16 or 39 nm on pyrite surface is affected by pyrite oxidation. Whereas these findings support the view that gold has strong affinity toward pyrite surface, a direct link between surface chemistry of crystallographic faces of pyrite and gold enrichment has not been established.

The reactivity of pyrite surfaces can be theoretically interpreted from the corresponding surface electronic structures (Rosso, 2001; Murphy and Strongin, 2009). Hung et al. (2002a, 2002b) revealed the surface geometry, energetics, and electronic structure of pyrite (1 0 0), (1 1 0), (2 1 0), and (1 1 1). Alfonso (2010) further investigated the surface stability of pyrite in different sulfur environments. Although these studies theoretically investigated the surface properties of pyrite, little information concerning the relation of surface reactivity to surface electronic structures was documented.

In this study, we present a comprehensive study, combining density functional theory (DFT) calculations with experiments, on the surface electronic structure and gold uptake of pyrite. The purpose of this study is to examine (1) the differences between surface electronic structure and the corresponding reactivity on different pyrite faces, and (2) the role of surface specific reactivity in understanding

the pyrite morphology indicative of gold enrichment. Our results provide strong evidence indicating that the high affinity of pyrite's {2 1 0} *form* to gold is closely related to the high energy state of the corresponding surface molecular orbitals and the resultant low Eh conditions. These findings may have far-reaching significance beyond gold mine prospecting because the concept of crystal-direction specific molecular orbital structure is universal for anisotropic materials and can be applied to any oriented mineral surface reactions including non-classical crystal growth, isotope fractionation during adsorption and mineralization, as well as biogenic mineral formation.

## 2. MATERIALS AND METHODS

### 2.1. Theoretical calculations

Simulated scanning tunneling microscopy (STM) images and electronic structures were calculated using DFT within the generalized-gradient approximation (GGA). For each surface, slab models with the lowest surface energy were employed, with all atoms being relaxed without fixation.

All DFT calculations in this study were performed using the Vienna *ab initio* simulation package (VASP) (Kresse and Furthmuller, 1996) along with projector augmented wave (PAW) method (Kresse and Joubert, 1999). Standard PAW pseudopotentials (Fe: $d^7s^1$, S: $s^2p^4$, and Au: $s^1d^{10}$) were used. PBE functions (Perdew et al., 1996) were utilized for the description of the exchange-correlation interaction among electrons. The electron-ion interactions were included within a plane wave basis with an energy cutoff of 350 eV, which gives good representation of physical properties of pyrite (Zhang et al., 2012). The convergence criteria for the total energy is $10^{-6}$. Hubbard $U$ correction (PBE + $U$) (Dudarev et al., 1998), which was verified to be well suited for the description of pyrite (Zhang et al., 2012; Krishnamoorthy et al., 2013; Zhang et al., 2015), was employed to treat the Fe 3$d$ electrons. A lattice constant of 5.423 Å and an indirect band gap of 0.95 eV for the bulk pyrite were obtained using a $U$-$J$ parameter of 1.6 eV (Krishnamoorthy et al., 2013), which are in good agreement with both the experimental data and previous calculations.

The structure models of typical stable pyrite facets were derived from the reported stability configuration in different sulfur environment (Alfonso, 2010). We employed the most stable slab models, *i.e.*, the {1 0 0}-S, {1 1 1}-3S, and {2 1 0}-2S′, to represent the surface electronic properties of pyrite (Fig. S1 in the Supplementary Information). The {1 0 0}-S is stoichiometric while the other two possess extra S atoms. All these symmetrical slab models were cut from the fully optimized bulk structure with unit cell and separated by a ~15 Å vacuum zone. Following the PBE + $U$ approach, the slab thicknesses was estimated to be approximately 25–27 Å, which gives a surface energy (Fig. S2 in the Supplementary Information) comparable to that from previous standard PBE results (Hung et al., 2002a, 2002b; Alfonso, 2010) and hence a good representation of the electronic structure (Zhang and Yates, 2012). The $k$-point sampling is generated by Monkhorst-Pack method (Monkhorst and Pack, 1976) with a 6 × 6 × 1 mesh for {1 0 0}, 5 × 5 × 1 for {1 1 1}, and 6 × 3 × 1 for {2 1 0} in the Brillouin zone.

We used supercells of pyrite {1 0 0}, {2 1 0}, and {1 1 1} faces to represent the reactivity of gold adsorption. (2 × 2), (2 × 1), and (1 × $\sqrt{3}$) slabs with 3 × 3 × 1, 3 × 3 × 1, and 4 × 2 × 1 $k$-point meshes were used for modeling {1 0 0}, {2 1 0}, and {1 1 1}, respectively. A series of tests were conducted on {1 0 0} surface to get the parameters for the adsorption modelling. The optimized energy cutoff is 400 eV and the slab thickness of {1 0 0} surface is 4 $FeS_2$ structural layers. Using these parameters, the total energy and adsorption energy of the gold-pyrite adsorption systems could converge to less than 0.001 eV and 0.03 eV, respectively. The same energy cutoff and similar slab thickness were employed for the gold adsorption on pyrite {2 1 0} and {1 1 1} faces.

### 2.2. Gold deposition experiments

The pyrite single crystals used in this study are the same as our previous study (Zhu et al., 2018). The {1 0 0} and {1 1 1} pyrite single crystals originated from the Navajun, La Rioja Province, Spain, while the {2 1 0} pyrite single crystals originated from Hunan Province, China. The miller index and micrographs of these pyrite faces, which can represent the crystallographic orientation dependent reactivity, were characterized by electron back-scattered diffraction (EBSD) and scanning electron micrographs (SEM) as shown in the supplementary materials of our previous study (Zhu et al., 2018).

To investigate the reactivity of single pyritic {1 0 0}, {1 1 1}, and {2 1 0} faces, the samples with the target surfaces were exposed to $HAuCl_4$ solutions while the other surfaces were coated with paraffin wax. To further examine the reactivity of distinguishable faces on complex *forms*, a section along [0 $k$ $l$] was cut from a cubic pyrite crystal, obtaining a combination sample with both (1 0 0) and (0 $k$ $l$) faces. The cut section surface was lightly wet polished with 600, 1000, and 1400 mesh grit silicon carbide paper and well washed with ultrapure water. Except for the surfaces of interest, the other surfaces on the sample were also screened with paraffin wax.

The $HAuCl_4$ deposition on pyrite surfaces were carried out in an anaerobic glove box made by MIKROUNA. Prior to immersion in the reaction solution, the exposed pyrite surfaces were washed by submerging the samples in an acid solution mixture of 48% HF, 70% $HNO_3$, and 99.99% acetic acid with a volume ratio of 1:2:1 for 30 s. Then the washed pyrite samples were immersed in 500 mg/L $HAuCl_4$ solution (within 1.0 M $Cl^-$ and pH = 3.25). The reactions were terminated by taking the samples out of the solutions after 5, 15, 25, 35, and 45 min and these samples were then characterized using X-ray photoelectron spectroscopy (XPS).

### 2.3. Characterization

The scanning electron microscopy and energy dispersion spectroscopy (SEM-EDS) were performed on a Hitachi SU8010 cold field emission SEM instrument operated at

20 kV. The samples were directly analyzed without any conductive coating. For EDS analysis, the working distance was set at 8.0 mm. XPS were performed on a Thermo Scientific K-Alpha XPS instrument equipped with an Al Kα source (1486.8 eV) operated at an emission current of 3 mA and a tube voltage of 12 kV. The vacuum in the analytical chamber was $<1 \times 10^{-8}$ mbar. To avoid the charged surface affecting the analysis, the Electron Neutralizer (flood gun) in the analysis chamber was enabled during the analysis processes. The energy resolution is 0.5 eV. XPS spectra were collected from three random selected area on each pyrite surface to estimate the experimental error. For the ion-milling experiments, a mild sputtering (1000 V $Ar^+$ ion energy at 10 mA electron emission current) was performed for 5 to 30 seconds on the samples exposed to $HAuCl_4$ solution. The XPS spectra were calibrated on the C 1s line of adventitious carbon contamination with a binding energy of 284.8 eV. The spectra were processed using the Thermo Avantage analysis software with regard for the smart background and the mixed Lorentz-Gaussian shapes of the peaks.

## 3. RESULTS

### 3.1. Crystal face specific gold deposition on pyrite

The kinetics of $Au^{3+}$ reductive precipitation from $HAuCl_4$ solutions onto individual crystal faces of natural pyrite single crystals were characterized using XPS and SEM-EDS. All irrelevant surfaces on the samples were sealed with paraffin wax to ensure the collected data only derived from the targeted crystal faces. The results unambiguously show that the highest precipitation rate is associated with the {2 1 0} while the slowest precipitation occurs on the {1 0 0} faces (Fig. 2a) and confirm that gold can indeed precipitate on pyrite surfaces (Fig. 2b–f).

The XPS spectra of Fe $2p_{3/2}$ and Au $4f$ core electrons for pyritic faces contacting with the $Au^{3+}$ chlorides solution are illuatrated in Fig. 3. From the Fe $2p_{3/2}$ spectra (Fig. 3a–c), the Fe—O species, which indicates the oxidation of pyrite coupled to the reduction of $Au^{3+}$, could be observed except for the bulk and two surface Fe states. From the Au $4f$ spectra (Fig. 3d–f), two types of gold species can be identified. One is assigned for the $4f_{7/2}$ at ~84.20 eV while the other is at ~85.00 eV. The former arises from metallic gold and the latter from $Au^+$ (Tauson et al., 2017). To further estimate the distribution of both Au species, we performed an ion-milling experiment with $Ar^+$-ion sputtering. The results (Fig. S3 in the Supplementary Information) show that the surface coverage of the $Au^+$ species is much thinner than that of the metallic gold, suggesting the $Au^+$ species may be bonded to surface S atoms on pyrite surfaces as a thin film. The Fe—O species in Fe $2p$ spectra (Fig. 3a–c), oxide O species (Fig. S4a in the Supplementary Information) and $SO_4^{2-}$ in S $2p$ spectra (Fig. S4b in the Supplementary

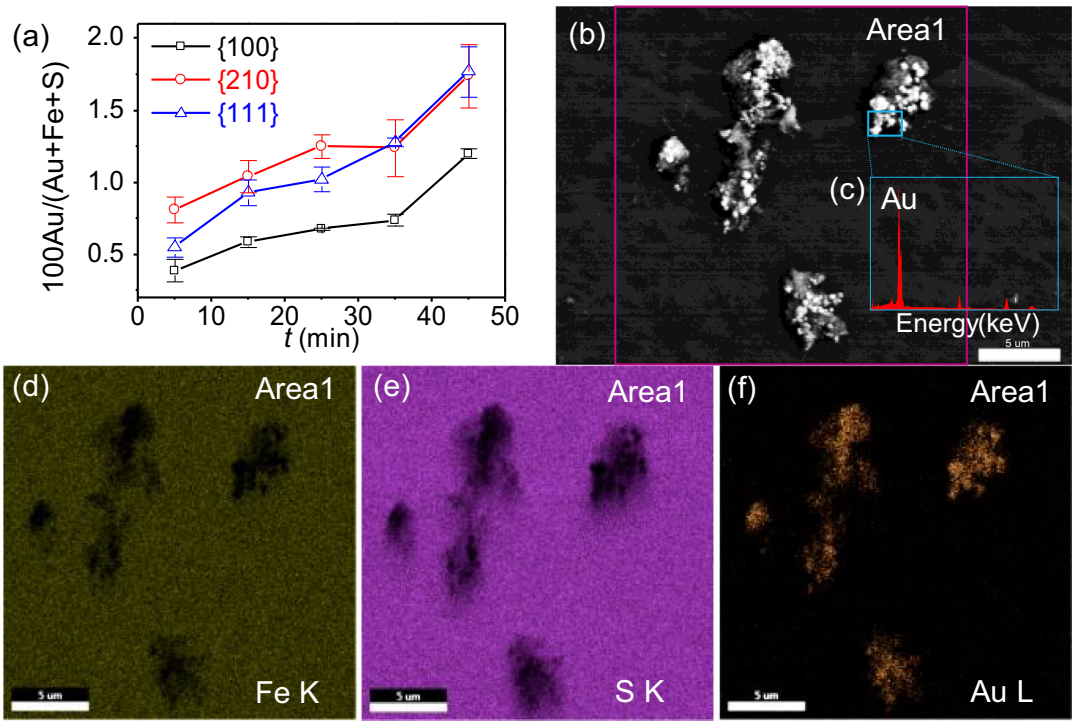


Fig. 2. (a) The gold concentrations of different pyrite surfaces exposed to the $HAuCl_4$ solution as functions of time. The error bars in (a) denote the standard deviation of X-ray photoelectron spectroscopy data from three randomly selected areas on the same sample. (b–f), SEM-EDS results of pyrite {1 0 0} face exposed to the $HAuCl_4$ solution after 45 min (c), the insert of (b), shows an EDS spectrum of a gold enriched area marked with a blue box. (d–f) are EDS mappings of Fe K, S K, and Au L for area1 marked with a purple box in (b). The scale bars in (b–f) represent 5 μm. (For interpretation of the references to colour in this figure legend, the reader is referred to the web version of this article.)

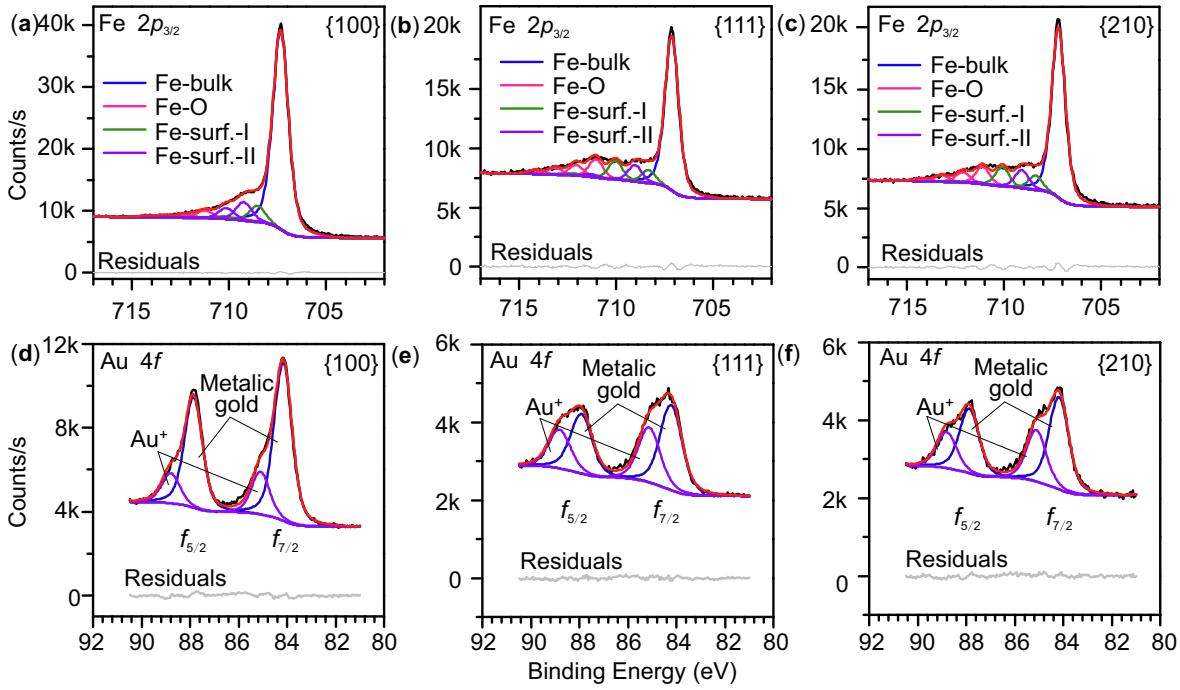


Fig. 3. XPS evidence for the reduction of Au(III) on pyrite surfaces. (a–c), The Fe $2p_{3/2}$ X-ray photoelectron spectra of different pyrite faces exposed to the $HAuCl_4$ solution after 45 min. The Fe-bulk peak was fitted as singlet state; The Fe-surf.-I peaks were fitted as quartet states; The Fe-surf.-II peaks were fitted as triplet states; The Fe—O peaks were fitted as quartet states. (d–f), The Au 4*f* X-ray photoelectron spectra of different pyrite surfaces exposed to the $HAuCl_4$ solution. All peaks of gold species were fitted by doublets with a 1:0.7 ($4f_{7/2}$: $4f_{5/2}$) height ratio, 3.70 eV apart, and with the same FWHM in each spectrum. All measurements were performed using an Al K$\alpha$ source.

Information) from pyrite {2 1 0} and {1 1 1} show much higher relative content than those from the {1 0 0}, which agrees with the surface structure dependent oxidation reactivity (Zhu et al., 2018).

Reductive precipitation experiment of $Au^{3+}$ chlorides on both pyritic {1 0 0} and {0 *k l*} faces show that, relative to that on the individual pyritic {1 0 0} and {0 *k l*} faces, the amount of gold precipitated on individual pyrite crystals enclosed by both the {1 0 0} and {0 *k l*} faces was about 1.5-times greater (Fig. 4).

### 3.2. Surface topography of typical pyrite faces

Air and ultra-high vacuum (UHV) STM images of pyrite {1 0 0} have been carried out despite pyrite cleaves poorly along the cubic planes (Eggleston and Hochella, 1990; Eggleston et al., 1996; Rosso et al., 1999; Rosso et al., 2000). However, compared to pyrite {1 0 0}, less work has been performed on other surfaces (Rosso, 2001). Using DFT calculations, we simulated the STM images of pyrite {1 0 0}, {2 1 0}, and {1 1 1}. The results, as shown in Fig. 5, illustrate 4-fold, 2-fold, and 3-fold symmetry for pyrite {1 0 0}, {2 1 0}, and {1 1 1}, which correspondingly consist with the two-dimensional atomic structures. Both Fe atoms and S-S bonds can be imaged with different contrast on the three surfaces. Distinguishable ridges and valleys can be identified in our simulated STM image, consisting with previous experimental STM

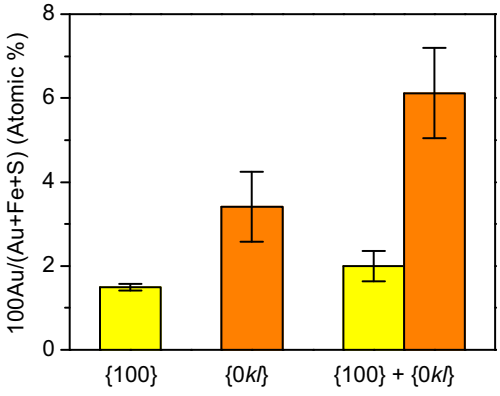


Fig. 4. The gold concentrations of individual {1 0 0}, {0 *k l*} and the combination surfaces exposed to the $HAuCl_4$ solution after 45 min. The error bars denote the standard deviation of X-ray photoelectron spectroscopy data from three randomly selected areas on the same sample.

images of pyrite {1 0 0} carried out on a growth surface which has been exposed to air for years (Eggleston and Hochella, 1990). However, the simulated STM image for pyrite {1 0 0} disagrees with those obtained in UHV cleaved surfaces (Rosso, 2001), which only presents the image of iron atoms. To elucidate the reason for this inconformity, we further simulated STM image for another

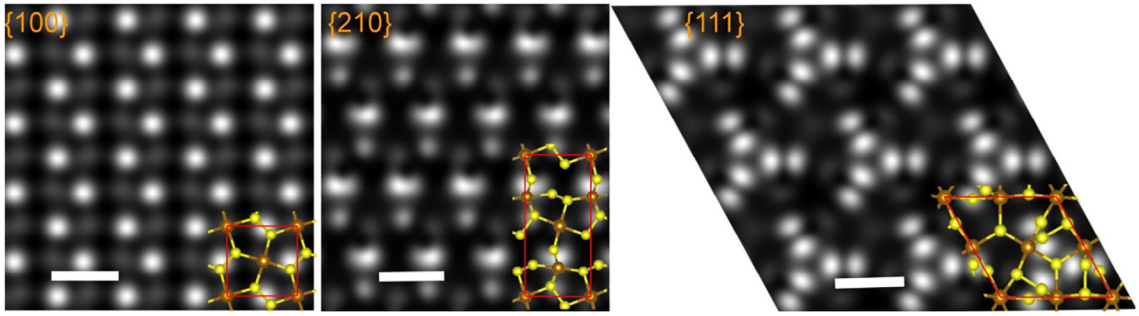


Fig. 5. Simulated STM images of pyrite {1 0 0}, {2 1 0}, and {1 1 1} surfaces using a bias of −0.5 eV. The tip distance is roughly 1.0 Å. The scale bars represent 5 Å.

metastable {1 0 0}-Fe surface without the outmost sulfur layer. The results (Fig. S5 in the Supplementary Information) display the same image with those obtained in UHV cleaved surfaces (Eggleston and Hochella, 1990). Therefore, we conclude that the models we used in this study can represent the most stable pyrite surfaces, and thereby interpret its surface reactivity.

### 3.3. Surface electronic structure of typical pyrite faces

Based on surface band structure calculations, the three pyrite faces show spin-dependent bands, with indirect band-gaps of 0.56, 0.15, and 0.28 eV for {1 0 0}, {2 1 0}, and {1 1 1}, respectively (Fig. 6). Two surface states in either majority or minority spin, which locate around conduction band (CB) and valence band (VB), respectively, can be identified from the three pyrite faces. These surface states locate at the highest occupied molecular orbital (HOMO) and the lowest unoccupied molecular orbital (LUMO). The energy level of HOMO and HOMO-LUMO gaps are in the same order of {2 1 0} > {1 1 1} > {1 0 0}, indicating that electrons on {2 1 0} surface are more easily excited than those on {1 1 1} and {1 0 0}.

Orbital projected density of states (PDOS) of pyrite {1 0 0}, {2 1 0}, and {1 1 1} surfaces present that most of the CB and VB are raised from Fe 3*d* orbital (Fig. 7). However, the contributions to the HOMO and LUMO, which consist of the two surface states, vary from pyrite {1 0 0} to {2 1 0} and {1 1 1} surfaces. The HOMO and LUMO of {1 0 0} surface mainly arise from Fe 3*d* orbital while those of the other two surfaces possess more contributions from S 3*p* orbital, as indexed by the green arrows in Fig. 7.

The presented spin polarizations in both band structure (Fig. 6) and DOSs (Fig. 7) are mainly around the first Fe layer (Fe1), as shown in Fig. 8. Compared to the spin polarization from Fe1, those from Fe2 to Fe3, and other bulk-like Fe layers are negligible, which agrees with the magnetic moment as labeled in Fig. 8 on the corresponding atoms. Sulfur atoms of the outmost layer on both {2 1 0} and {1 1 1} possess spin polarization in certain degree while those on {1 0 0} does not have, which is consistent with previous calculations performed on {1 0 0} surface (Zhang et al., 2012). These spin polarization of S atoms on {2 1 0} and {1 1 1} could be the reason for the S 3*p* contributions locating at surface states as described above. The surface magnetic moments for the outmost Fe atoms on

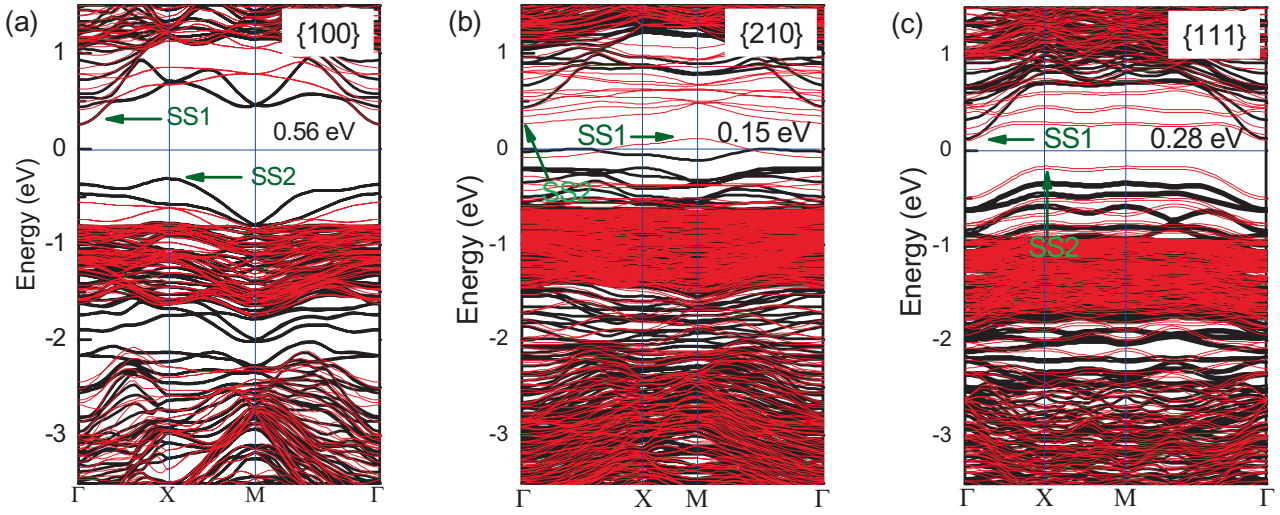


Fig. 6. Band structure of pyrite (a) {1 0 0}, (b) {2 1 0}, and (c) {1 1 1} surfaces. Bold black and thin red lines denote states in the majority and minority spin channels, respectively. Arrows highlight the two surface states (denoted SS1 and SS2) that determine the surface highest occupied molecular orbital (HOMO) and the lowest unoccupied molecular orbital (LUMO) gap. (For interpretation of the references to colour in this figure legend, the reader is referred to the web version of this article.)

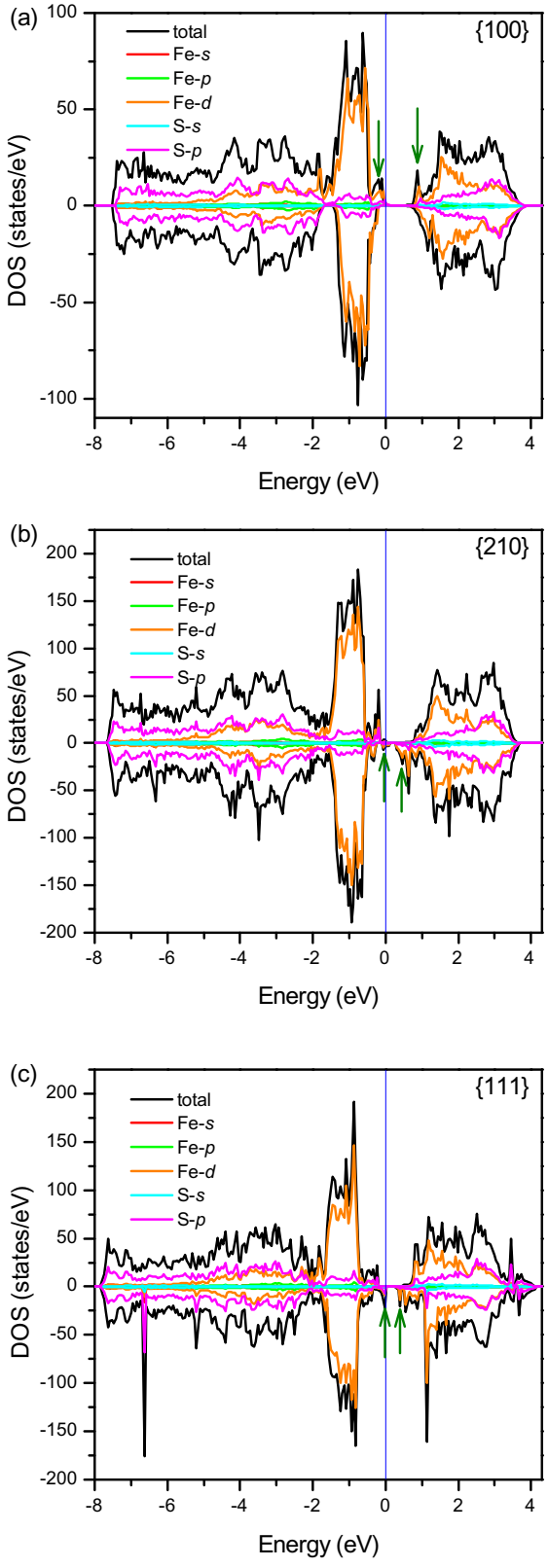


Fig. 7. Projected density of states (PDOS) of pyrite (a) {1 0 0}, (b) {2 1 0}, and (c) {1 1 1} surfaces. The green arrows in the PDOSs donate the surface states locating at the HOMO and LUMO. (For interpretation of the references to colour in this figure legend, the reader is referred to the web version of this article.)

pyrite {1 0 0}, {2 1 0}, and {1 1 1} are 1.97, 2.75, and 1.15 $\mu_B$, respectively. Depth resolved magnetic moment (Fig. 9), display that the magnetic moment change only occurs in the limit depth of 2.8 Å, 3.6 Å, and 3.2 Å for {1 0 0}, {2 1 0}, and {1 1 1}, respectively. Furthermore, the magnetic moment changes of both Fe and S atoms on {2 1 0} surface are the largest among the three faces, indicating {2 1 0} face possesses the highest spin polarization and the deepest surface effect.

To further investigate the surface effect on pyrite surfaces, depth-resolved electronic structures of pyrite surfaces are presented through the Fe-3*d* PDOS spectra from different surface Fe layers, which are displayed in Fig. 10. Surface effect is limited in the top two (for {1 0 0} and {1 1 1}) or five (for {2 1 0}) Fe atomic layers (~7 Å in total thickness). Combining the surface effect of magnetic moment (~3 Å) with that of the Fe-3*d* PDOS spectra (~7 Å), one can observe that the surface effect is limited in about 7 Å while only atoms in half depth mainly contribute to surface states.

The net charges of atoms from the {1 0 0}, {2 1 0}, and {1 1 1} surfaces are deciphered by Bader charge-division scheme (Bader, 1990; Henkelman et al., 2006), as shown in Fig. 11. Compared to the bulk like atoms, surface Fe lose ~0.1 (for {1 0 0} and {1 1 1}) or 0.27 (for {2 1 0}) electrons while surface S atoms can either gain or lose electrons in certain degree. The surface S of {1 0 0} only lose 0.02–0.07 electrons while those of {2 1 0} and {1 1 1} can either gain or lose more than 0.1 electrons. These differences could be assigned to the extra S atoms on {2 1 0} and {1 1 1}.

Work functions ($\varphi$), ionization potential ($I$), and electron affinity ($\chi$) can be calculated based on the band structure and vacuum energy level of pyrite {1 0 0}, {2 1 0}, and {1 1 1} surfaces (Fig. S6 in the Supplementary Information). The results (Table 1) show that $I$ for the three pyrite faces is in the order of {2 1 0} < {1 0 0} < {1 1 1} while $\varphi$ and $\chi$ in the order of {1 0 0} < {2 1 0} < {1 1 1}. The band energy level shows that the energy level of {1 1 1} is the lowest among the three faces, indicating {1 1 1} face possesses the highest reducibility.

### 3.4. Adsorption energy and configurations of gold atom on typical pyrite faces

To characterize the interaction of gold on pyrite surfaces, the adsorption energy of gold on pyrite {1 0 0}, {2 1 0}, and {1 1 1} surfaces were calculated. All the possible adsorption sites on pyrite surfaces were considered as listed in Table 2. The most stable adsorption configurations (Fig. 12) show that the coordination number of the adsorbed gold atom for {1 0 0} is 1 while that for {2 1 0} and {1 1 1} is 3. Although the gold atoms on both {2 1 0} and {1 1 1} interact with three S atoms, the S—Au bond length varies from one to another (Table 2). The S—Au bond lengths for {2 1 0} vary from 2.32 to 2.64 Å while those for {1 1 1} are almost the same (2.42 Å). The adsorption energies of the most stable configurations are in the order of {2 1 0} (−3.25 eV) < {1 1 1} (−3.08 eV) < {1 0 0} (−2.26 eV), indicating gold adsorption on the {2 1 0} surface is the most stable one among the three surfaces.

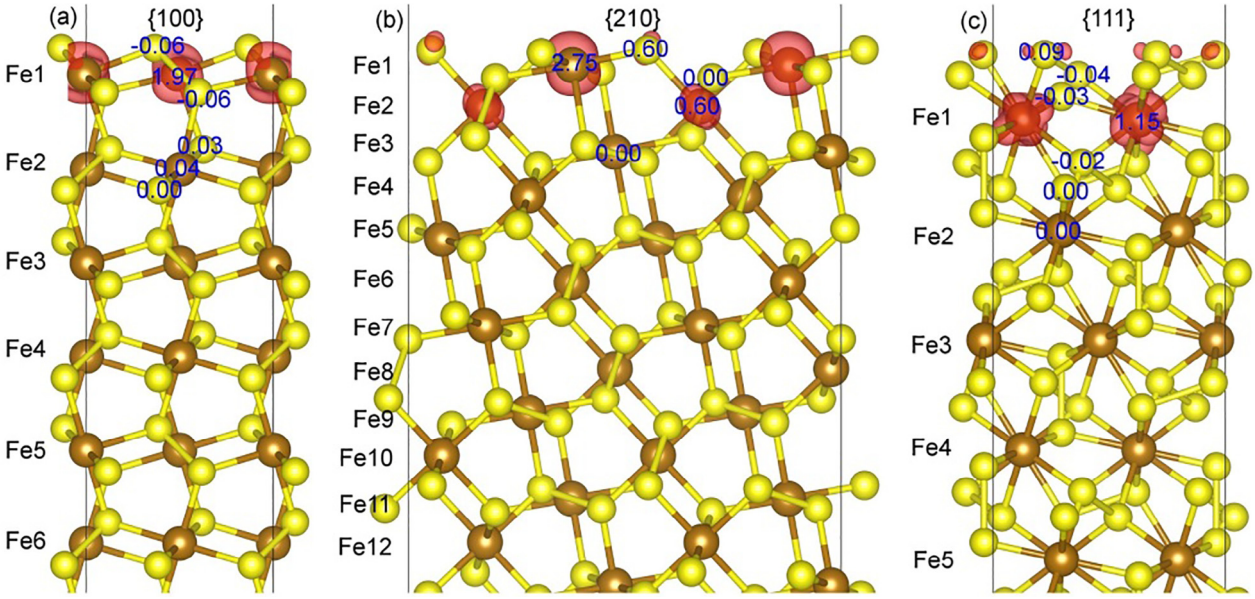


Fig. 8. Isosurfaces of spin density of pyrite (a) {1 0 0}, (b) {2 1 0}, and (c) {1 1 1} surfaces. The magnetic moment ($\mu_B$) values represent the spin polarization on the corresponding atom. The white yellow and brown spheres represent sulfur and iron atoms, respectively. (For interpretation of the references to colour in this figure legend, the reader is referred to the web version of this article.)

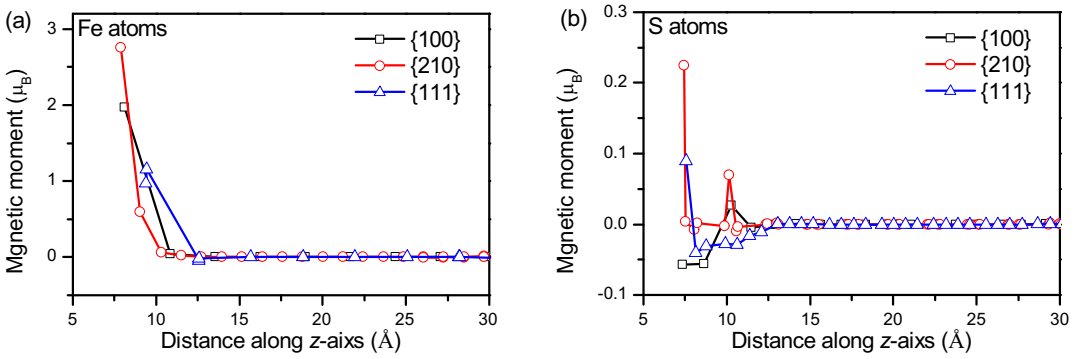


Fig. 9. Magnetic moment distribution of (a) Fe and (b) S atoms along z-axis of pyrite {1 0 0}, {2 1 0}, and {1 1 1} surfaces.

## 4. DISCUSSION

### 4.1. Surface electronic structure determined reactivity on single-crystal face of pyrite

Based on the surface electronic structure difference, we can discuss the reactivity of single-crystal faces of pyrite on both thermodynamics and kinetics aspects. On thermodynamics, the electronic structure-controlled surface potential (Fig. 13) can be employed to identify the direction of certain redox reactions. When all the surface potentials are integrated versus standard hydrogen electrode (SHE), one can get the electrode potential of different pyrite surfaces, such that

$$\mathrm{py}\{100\} \rightleftharpoons \text{oxidized-py}\{100\} + \mathrm{e}\left(E^0 = +0.55\ \mathrm{V}\right), \quad (1)$$

$$\mathrm{py}\{210\} \rightleftharpoons \text{oxidized-py}\{210\} + \mathrm{e}\left(E^0 = +0.93\ \mathrm{V}\right), \quad (2)$$

$$\mathrm{py}\{111\} \rightleftharpoons \text{oxidized-py}\{111\} + \mathrm{e}\left(E^0 = +1.36\ \mathrm{V}\right). \quad (3)$$

After the electrode potentials are obtained, one can easily judge whether a reaction can occur spontaneously or not. For instance, because all the electrode potentials of the three faces are greater than zero, *i.e.*, the SHE, $H_2$ can reduce the pyrite surfaces.

Although thermodynamics can predict the occurrence of certain reactions on certain thermodynamic conditions, the reaction rate, $r$, could not be predicted directly. On the one hand, using transition state model (TST), the rate of geochemical reactions could be described through an $r$ - $\Delta G$ relationship (Lasaga, 1998). Based on the adsorption energies of gold on pyrite surfaces (Table 2), it can be inferred that the adsorption rate of gold on pyrite {2 1 0} could be the highest among the three faces. On the other hand, the kinetics can be interpreted by the HOMO-LUMO gap. Because the {2 1 0} faces possess the narrowest gap, the electrons on the {2 1 0} surfaces are much easier excited than those on the other surfaces, which can lead to higher reaction rate. Therefore, the {2 1 0} face should possess

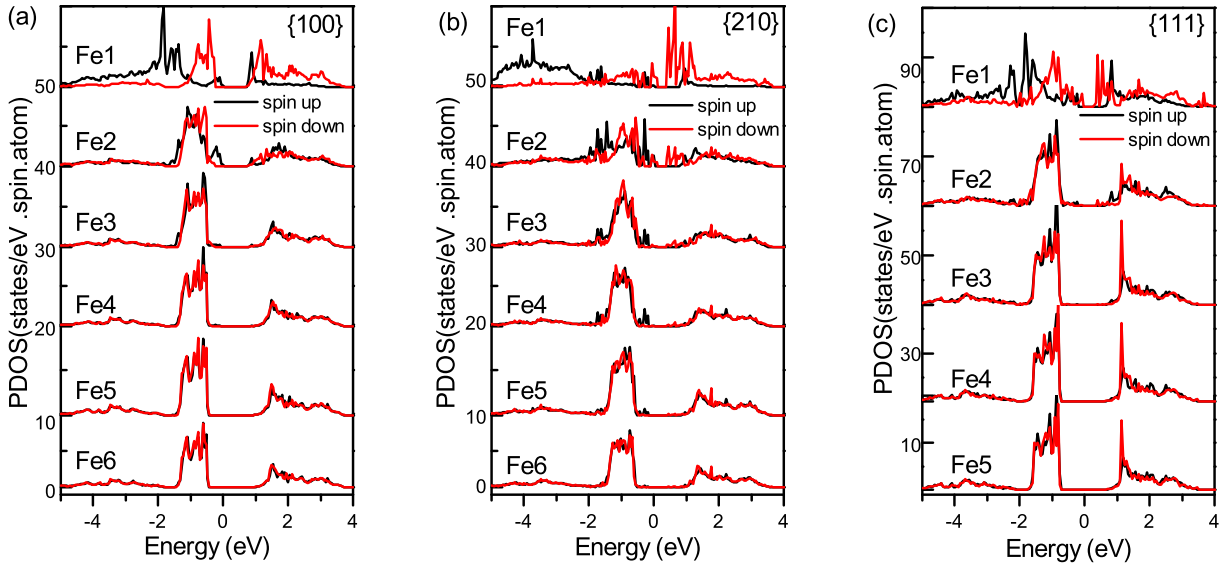


Fig. 10. Projected density of states (PDOS) for Fe-3*d* orbital in different layers of pyrite(a) {1 0 0}, (b) {2 1 0}, and (c) {1 1 1}. The labeled Fe layer numbers are in line with those in Fig. 8. Bold black and thin red lines in the PDOS spectra denote states in the majority and minority spin channels, respectively. (For interpretation of the references to colour in this figure legend, the reader is referred to the web version of this article.)

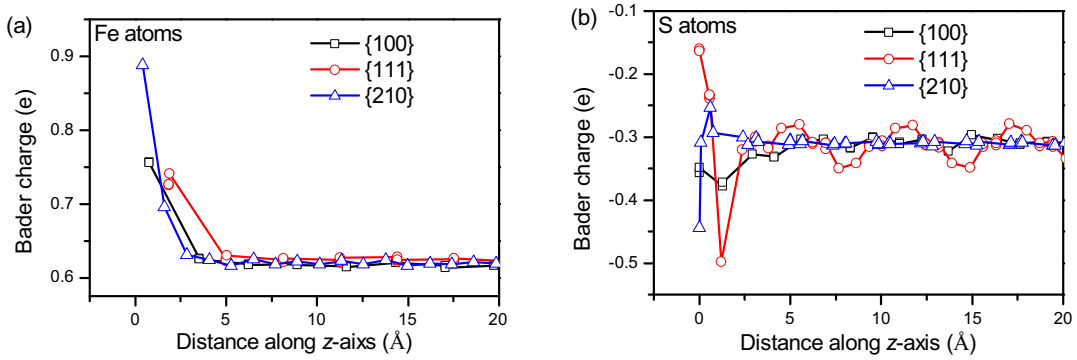


Fig. 11. Bader charge distribution of (a) Fe and (b) S atoms along *z*-axis of pyrite {1 0 0}, {2 1 0}, and {1 1 1} surfaces.

Table 1
Calculated work functions ($\varphi$), ionization potential ($I$), and electron affinity ($\chi$) of pyrite {1 0 0}, {2 1 0}, and {1 1 1} surfaces (eV).

| Surfaces | {1 0 0} | {2 1 0} | {1 1 1} |
|---|---|---|---|
| $I$ | 5.26 | 5.22 | 5.92 |
| $\varphi$ | 4.95 | 5.33 | 5.76 |
| $\chi$ | 4.70 | 5.07 | 5.66 |

higher reactivity than the other faces when redox reactions occurring on pyrite surfaces.

### 4.2. Surface potential difference induced reactivity shift on complex crystal pyrite face

Most of natural pyrite crystals always contain complex shapes instead of single-crystal *forms* (Murowchick and Barnes, 1987). Because the electronic structure of pyrite faces shows that these faces can be described as metal ({2 1 0}) or semiconductor ({1 1 1} and {1 0 0}) with certain band gap, we employ the band bending concept, which was initially introduced to describe the metal and semiconductor contact (Zhang and Yates, 2012), to describe the electronic structure of complex pyrite crystals. When different faces occur on a same pyrite crystal, the band bending occurs as the Fermi levels of various faces shift to the same level (Fig. 14). When {2 1 0} and {1 0 0} occur on one pyrite crystal (Fig. 14a), the electrons will flow from {1 0 0} to {2 1 0}. The electron transfer will continue until the Fermi levels of {2 1 0} and {1 0 0} are aligned. Consequently, {1 0 0} possess higher potential than {2 1 0}. Similar to {2 1 0} + {1 0 0}, the couples of {2 1 0} + {1 1 1} (Fig. 14b) and {1 0 0} + {1 1 1} (Fig. 14c) also possess potential difference between the faces.

Once the potential difference forms between various faces, the surface reactivity can be linked to the bulk conduction model (Yanina and Rosso, 2008). Fig. 15a

Table 2
Comparison of coordination number, bond length, and adsorption energy of an adsorbed gold atom on pyrite {1 0 0}, {1 1 1}, and {2 1 0} surfaces using DFT + $U$ calculations.

| Sites | Coordination number | S-Au/Fe-Au Bond length (Å) | Adsorption Energy (eV) |
|---|---|---|---|
| {1 0 0}-**Fe** | **1** | **2.50 (Fe-Au)** | **−2.26** |
| {1 0 0}-S | 1 | 2.31 (S-Au) | −1.54 |
| {2 1 0}-S1 | 1 | 2.26 (S-Au) | −2.91 |
| {2 1 0}-**S2** | **3** | **2.40; 2.32; 2.64 (S-Au)** | **−3.25** |
| {2 1 0}-Fe | 1 | 2.44 (Fe-Au) | −2.22 |
| {1 1 1}-S1 | 1 | 2.32 (S-Au) | −2.50 |
| {1 1 1}-**S2** | **3** | **2.41; 2.42; 2.42 (S-Au)** | **−3.08** |

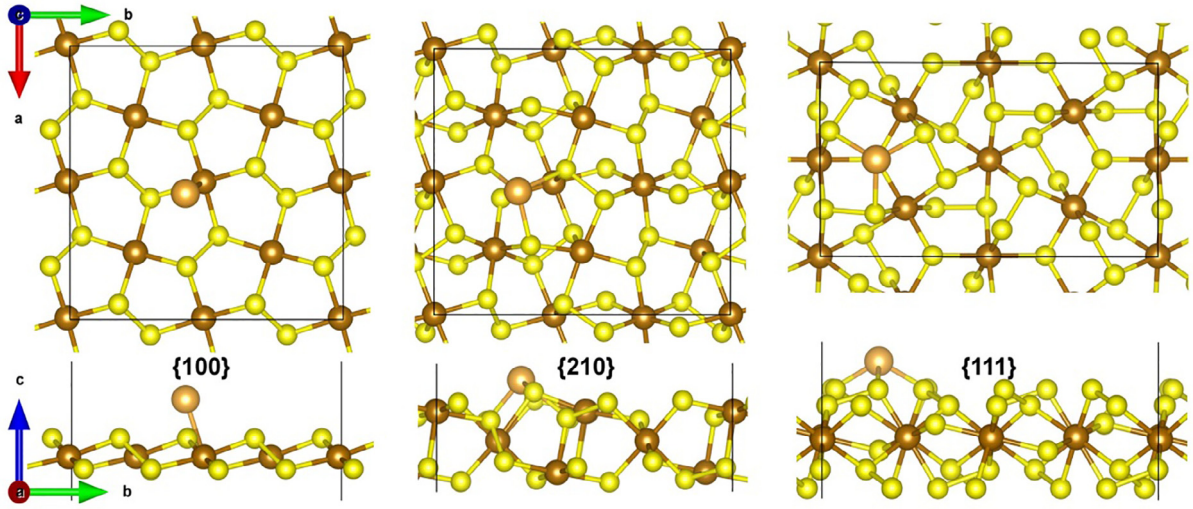


Fig. 12. The most stable relaxed configurations of gold interaction with pyrite {1 0 0}, {2 1 0}, and {1 1 1} surfaces. The white yellow, brown and white brown spheres represent sulfur, iron and gold atoms, respectively. (For interpretation of the references to colour in this figure legend, the reader is referred to the web version of this article.)

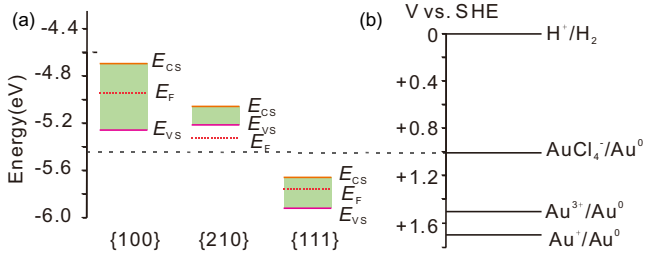


Fig. 13. Absolute energy scale of (a) pyrite {1 0 0}, {2 1 0}, and {1 1 1} surfaces and (b) several gold redox couples. $E_V$, vacuum energy; $E_F$, Fermi energy; $E_{CB}$, energy of conduction band minimum for bulk; $E_{VB}$, energy of valence band maximum for bulk; $E_{CS}$, energy of conduction band minimum for surface; $E_{VS}$, energy of valence band maximum for surface.

illustrates the possible conduction model in pyrite crystals. Pyrite {1 0 0} possess higher potential than {2 1 0} and {1 1 1}, when reactant occurs on pyrite surfaces, the reductant and oxidant may be separated on different faces through the bulk crystal conduction. A similar separation of redox reactions on anatase {0 0 1} and {0 1 1} was observed by Ohno et al. (2002). Therefore, beyond reactivity on single-crystal faces, the bulk conduction model can enhance the reactivity among various pyrite faces. And this is the reason for the enhanced reactivity of gold deposition onto combined surfaces, as shown in the schematic diagram (Fig. 15b–d) illustrating enhanced gold enrichment in pyrite crystals of complex *forms*.

### 4.3. Linking gold enrichment to pyrite face specific reactivity and shapes

Based on the electrode potential of gold species (Haynes, 2014):

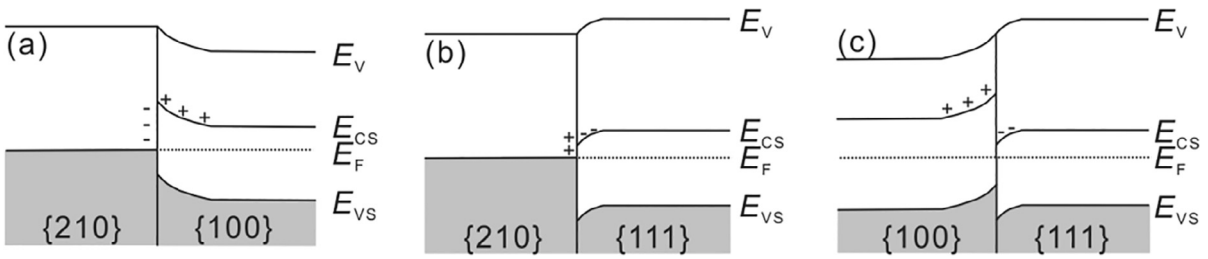


Fig. 14. Energy band diagrams of surface dimer combination among pyrite {1 0 0}, {2 1 0}, and {1 1 1} surfaces. All the variables in the diagrams are the same with those in Fig. 13.

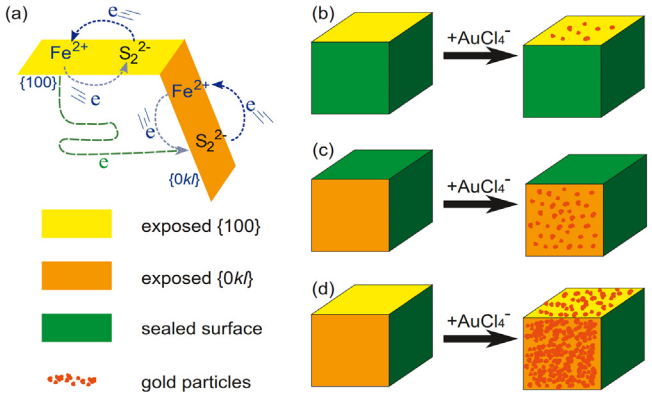


Fig. 15. (a) Electron transfer routes between {1 0 0} and {0 *k l*} surfaces of pyrite with combination form. (b and c) Schematic diagram summarizing the gold deposition behavior for individual {1 0 0}, {0*kl*}, and the combination surfaces.

$$AuBr_4^- + 3e \rightleftharpoons Au + 4Br^- \left(E^0 = +0.854\ V\right), \quad (4)$$

$$AuBr_2^- + e \rightleftharpoons Au + 2Br^- \left(E^0 = +0.959\ V\right), \quad (5)$$

$$AuCl_4^- + 3e \rightleftharpoons Au + 4Cl^- \left(E^0 = +1.002\ V\right), \quad (6)$$

$$Au^{3+} + 3e \rightleftharpoons Au \left(E^0 = +1.498\ V\right), \quad (7)$$

$$Au^{+} + e \rightleftharpoons Au \left(E^0 = +1.692\ V\right), \quad (8)$$

and the observed face dependent surface electrode potential in this study, one can easily identify that gold complex species can be reduced to metal gold on pyrite surfaces, which was first experimentally confirmed by Hyland and Bancroft (1989).

Both theoretical and experimental results reinforce the viewpoint that the crystal face dependent reactivity of pyrite is an intrinsic driving force of gold enrichment on pyrite with specific crystal morphology. In gold-bearing liquids, ionic gold prefers to precipitate on pyritic {2 1 0} faces in response to the high surface reactivity. On the one hand, the precipitation of gold can lower the surface energy of all pyrite faces to decrease the growth rate of pyrite faces, suggesting that gold precipitation on pyrite surfaces may lead to crystal sizes smaller than those grown without gold precipitation. This may be one important reason for the observed gold enrichment in fine pyrite crystals (Tauson et al., 2014; Tauson et al., 2018) that has traditionally been attributed to the occurrence of large specific surface area On the other hand, the precipitation of gold can improve the stability of the {2 1 0} faces, compared with those of the {1 0 0} and {1 1 1}, as the adsorption energy of a gold atom on pyrite {2 1 0} is the lowest among the habitual crystal faces of pyrite as described above. This means that gold on the {2 1 0} faces can decrease the growth rate of the {2 1 0} faces, ultimately resulting in a correlation

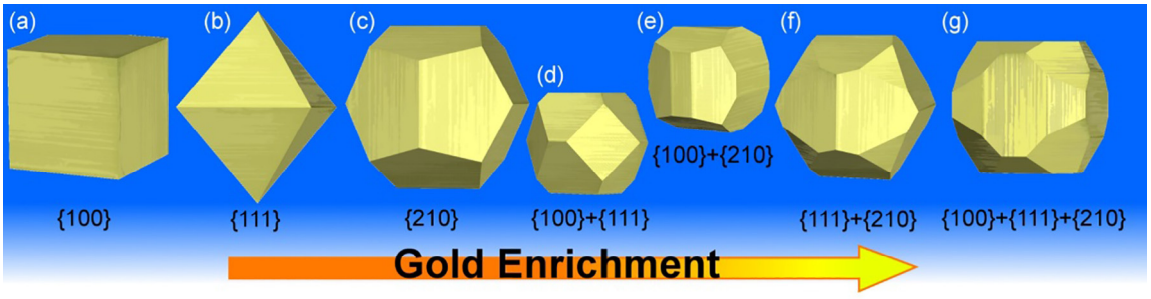


Fig. 16. Predicted pyrite shape evolution for the gold enrichment through its surface electronic structure and reactivity.

between gold content in the ore rock and the occurrence of pyritohedral {2 1 0} and complex *forms* of pyrite crystals. Furthermore, the intrinsic reactivity of pyrite faces is practicable not only to gold but also to all other components of a system as well periodically changing their composition through geological times, which may be the fundamental for understanding some crystallographic orientation related geological phenomenon.

Based on the facts that (1) pyrite complex *forms* possess higher reactivity than single-crystals and (2) the redox reactivity of pyrite faces is in order of {2 1 0} > {1 1 1} > {1 0 0}, the reactivity of gold adsorption/reduction on pyrite should approximately be in the order of {1 0 0} < {1 1 1} < {2 1 0} < {1 0 0} + {1 1 1} < {1 0 0} + {2 1 0} < {1 1 1} + {2 1 0} < {1 0 0} + {1 1 1} + {2 1 0}. This order is in line with the statistic law for the gold enrichment in complex pyrite forms (Chen et al., 1987; Shen et al., 2013). Thus, it infers that the gold enrichment, as illustrated in Fig. 16, is indeed linked to the surface gold reductive deposition and the corresponding shapes.

### 4.4. Implications for the crystal face specific geochemistry

Anisotropy is a fundamental property of crystalline materials and in many cases a determinant physical trait for crystal application (e.g. birefringence and piezoelectricity). Extensive studies over the past two decades in the reactivities of solid-fluid interfaces (Brown, 2001; Yanina and Rosso, 2008) further documented that the anisotropy can manifest as crystallographic direction-specific chemical reactions. Such reactions include preferential incorporation of elements in different crystal facets and the development of intersectoral zoning (Paquette and Reeder, 1990; Paquette and Reeder, 1995), face-specific surface energetics (Hong and Teng, 2014), oriented surface binding of organic molecules (Teng et al., 2006), and oriented nanocluster aggregation (Banfield et al., 2000). To date, such advances already find application in various fields such as catalysis (Pan et al., 2011), biomineralization (Killian et al., 2009) and medical research (Olszta et al., 2007). Pyrite face specific gold deposition presented in this study and the crystal face specific pyrite oxidation from our previous study (Zhu et al., 2018) showcase the practical importance of crystal face-specific reactivity in economic geology. Pyrite-water interactions are also hypothesized to have played an important role in the origin of life. For example, the "iron-sulfur world" (ISW) scenario (Wächtershäuser, 1992) is an interesting proposal for prebiotic chemical reactions (Boehme and Marx, 2003) as study found pyrite {1 0 0} surfaces were able to act as catalysts in the processes of peptide synthesis (Schreiner et al., 2008).

A conspicuous knowledge gap appears to exist concerning the effect of crystal anisotropy on isotope geochemistry as the orientation effects were found to be of importance for isotope measurements (Huberty et al., 2010). It has been long recognized that surface reactivity of minerals influences the isotope fractionation during mineral-water interactions (Cole et al., 1983). On the one hand, this is because isotopic equilibrium fractionation between mineral and fluid is controlled by the surface ion exchange and diffusion (Guilbaud et al., 2011). On the other hand, it is shown that precipitation and adsorption reactions at mineral-water interface can also affect the isotopic fractionation (Beard et al., 2010; Guilbaud et al., 2010). However, many proposed reactions that cause isotopic fractionation at mineral-water interfaces ignore the anisotropic surface reactivity of minerals. This oversight may lead to misunderstanding of the isotopic fractionations, especially those resulting from kinetic effects, at mineral-water interfaces. Based on the observations of anisotropic gold deposition on pyrite crystal faces presented in this study, we suspect that distinct fractionation may occur for S and Fe when pyrite mineralizes in different environment and expresses different crystal habits. We further speculate that such morphological dependence of fractionation may be universal for any minerals with strong anisotropic reactivities.

## 5. CONCLUDING REMARKS

The crystal face dependent surface electronic structure of pyrite {1 0 0}, {2 1 0}, and {1 1 1} was investigated using DFT calculations. Surface states, which narrow the surface band gap, were observed on all the considered pyrite faces. The HOMO-LUMO gaps of pyrite {1 0 0}, {1 1 1}, and {2 1 0} faces are 0.56, 0.28, and 0.15 eV, respectively. While the bulk pyrite is nonmagnetic, the topmost Fe layers of pyrite {1 0 0}, {1 1 1}, and {2 1 0} faces are spin polarized, with magnetic moments of 1.97, 1.15, and 2.75 per Fe atom. The surface effect affects the top 7 Å of these pyrite surfaces while only the topmost ~3 Å mainly contribute to the surface states. The electrode potentials of the pyrite {1 0 0}, {1 1 1}, and {2 1 0} faces are 0.55, 0.93, and 1.36 V (*vs.* SHE), respectively.

Furthermore, based on the electronic structure of these pyrite surfaces, the reactivity of pyrite single-crystal and complex crystal faces was analyzed. Electrons on individual {2 1 0} surface are easier to be excited than those on the other surfaces. The surface potential difference of complex crystal faces can enhance the reactivity through the bulk conduction model proposed by Yanina and Rosso (2008). These theoretical predictions are confirmed by kinetic measurements of gold reductive deposition on pyrite surfaces.

Finally, combined theoretical with experimental results, the reactivity of gold adsorption/reduction on pyrite crystal faces was observed in the order of {1 0 0} < {1 1 1} < {2 1 0} < {1 0 0} + {1 1 1} < {1 0 0} + {2 1 0} < {1 1 1} + {2 1 0} < {1 0 0} + {1 1 1} + {2 1 0}, which agrees well with the statistic law for the gold enrichment in pyrite complex crystals. Thus, the shape of gold-bearing pyrite is linked to the gold enrichment; and the predicted shape evolution from low to high gold accumulation is in order of cube, octahedron, pyritohedron, and other complex polyhedron with {2 1 0} faces, such as cubi-pyritohedron.

These results afforded evidence supporting the view that the intrinsic surface chemistry of pyrite is an important fundamental factor controlling the occurrence of specific pyrite shapes, exemplifying the significance of crystal face specific-reactivity in understanding ore mineral formation. The crystal face dependent reactivity of pyrite not only exposes the underlining physicochemical principles of gold enrichment

in pyrite but emphasizes the critical role of highly reactive crystal faces in controlling geochemical processes. The concerted enhancing effect by band bending and galvanic cell on surface reactivity may be a widely occurring phenomenon in semiconductor minerals and photoelectric minerals. Meanwhile, the difference in molecular orbitals in different crystal faces may be used to explore any oriented mineral surface reactions such as biomineralization and adsorption/crystallization related isotope geochemistry.

## ACKNOWLEDGMENTS

We thank Parker, S. C. from University of Bath for helpful discussions on the calculation results; Q. Zhou and H. M. Liu from GIGCAS in Guangzhou for SEM-EDS and XPS analysis, respectively. This study is supported by the fund from the Ministry of Science and Technology of the People's Republic of China (2016YFC0600103) and the National Natural Science Foundation of China (Grant No. 41573112 and 41702042), the China Postdoctoral Science Foundation (No. 2018M643220 and 2019T120755) and the Science and Technology Planning Project of Guangdong Province, China (Grant No. 2017B030314175). This is contribution No. IS-2738 from GIG-CAS.

## APPENDIX A. SUPPLEMENTARY MATERIAL

Supplementary data to this article can be found online at https://doi.org/10.1016/j.gca.2019.08.011.

## REFERENCES

Alfonso D. R. (2010) Computational investigation of $FeS_2$ surfaces and prediction of effects of environment on stabilities. *J. Phys. Chem. C* **114**, 8971–8980.

Bader R. F. (1990) *Atoms in Molecules*. Wiley Online Library.

Banfield J. F., Welch S. A., Zhang H. Z., Ebert T. T. and Penn R. L. (2000) Aggregation-based crystal growth and microstructure development in natural iron oxyhydroxide biomineralization products. *Science* **289**, 751–754.

Beard B. L., Handler R. M., Scherer M. M., Wu L., Czaja A. D., Heimann A. and Johnson C. M. (2010) Iron isotope fractionation between aqueous ferrous iron and goethite. *Earth Planet. Sci. Lett.* **295**, 241–250.

Brown, Jr., G. E. (2001) How minerals react with water. *Science* **294**, 67–69.

Boehme C. and Marx D. (2003) Glycine on a wet pyrite surface at extreme conditions. *J. Am. Chem. Soc.* **125**, 13362–13363.

Cabri L. J., Newville M., Gordon R. A., Crozier E. D., Sutton S. R., McMahon G. and Jiang D. T. (2000) Chemical speciation of gold in arsenopyrite. *Can. Mineral.* **38**, 1265–1281.

Cai Y. J. and Zhou M. (1994) Crystalomorphological characteristics of pyrite in hydrothermal gold deposit. *Sci. China Ser. B-Chem.* **37**, 117–128.

Chen G. (1987) *Genetic Mineralogy and Prospecting Mineralogy*. Chongqing Press, Chongqing..

Chen G., Sun D., Zhang L., Zang W., Wang J. and Lu A. (1987) Morphogenesis of pyrite. *Geoscience* **1**, 60–76.

Cole D. R., Ohmoto H. and Lasaga A. C. (1983) Isotopic exchange in mineral-fluid systems. I. Theoretical evaluation of oxygen isotopic exchange accompanying surface reactions and diffusion. *Geochim. Cosmochim. Acta* **47**, 1681–1693.

Cook N. J. and Chryssoulis S. L. (1990) Concentrations of invisible gold in the common sulfides. *Can. Mineral.* **28**, 1–16.

Dudarev S. L., Botton G. A., Savrasov S. Y., Humphreys C. J. and Sutton A. P. (1998) Electron-energy-loss spectra and the structural stability of nickel oxide: an LSDA+U study. *Phys. Rev. B* **57**, 1505–1509.

Eggleston C. M., Ehrhardt J. J. and Stumm W. (1996) Surface structural controls on pyrite oxidation kinetics: An XPS-UPS, STM, and modeling study. *Am. Mineral.* **81**, 1036–1056.

Eggleston C. M. and Hochella M. F. (1990) Scanning tunneling microscopy of sulfide surfaces. *Geochim. Cosmochim. Acta* **54**, 1511–1517.

Elsetinow A. R., Guevremont J. M., Strongin D. R., Schoonen M. A. A. and Strongin M. (2000) Oxidation of {100} and {111} surfaces of pyrite: effects of preparation method. *Am. Mineral.* **85**, 623–626.

Fu Y., Nie X., Qin Z., Li S. and Wan Q. (2017) Effect of particle size and pyrite oxidation on the sorption of gold nanoparticles on the surface of pyrite. *J. Nanosci. Nanotechnol.* **17**, 6367–6376.

Goldfarb R., Baker T., Dube B., Groves D. I., Hart C. J. R. and Gosselin P. (2005) Distribution, character and genesis of gold deposits in metamorphic terranes. In Economic geology 100th Anniversary volume (eds. J. W. Hedenquist, J. F. H. Thompson, R. G. Goldfarb, and J. P. Richards). Society of Economic Geologists, Littleton, Colorado, USA. pp. 407–450. Available at: https://researchonline.jcu.edu.au/996/ [Accessed October 10, 2017].

Guevremont J. M., Elsetinow A. R., Strongin D. R., Bebie J. and Schoonen M. A. A. (1998) Structure sensitivity of pyrite oxidation: comparison of the (100) and (111) planes. *Am. Mineral.* **83**, 1353–1356.

Guilbaud R., Butler I. B., Ellam R. M., Rickard D. and Oldroyd A. (2011) Experimental determination of the equilibrium Fe isotope fractionation between $Fe^{2+}_{aq}$ and $FeS_m$ (mackinawite) at 25 and 2°C. *Geochim. Cosmochim. Acta* **75**, 2721–2734.

Guilbaud R., Butler I. B., Ellam R. M. and Rickard D. (2010) Fe isotope exchange between $Fe(II)_{aq}$ and nanoparticulate mackinawite ($FeS_m$) during nanoparticle growth. *Earth Planet. Sci. Lett.* **300**, 174–183.

Haynes W. M. (2014) *CRC Handbook of Chemistry and Physics*, 95th ed. CRC Press.

Henkelman G., Arnaldsson A. and Jonsson H. (2006) A fast and robust algorithm for Bader decomposition of charge density. *Comput. Mater. Sci.* **36**, 354–360.

Hong M. and Teng H. H. (2014) Implications of solution chemistry effects: direction-specific restraints on the step kinetics of calcite growth. *Geochim. Cosmochim. Acta* **141**, 228–239.

Huberty J. M., Kita N. T., Kozdon R., Heck P. R., Fournelle J. H., Spicuzza M. J., Xu H. and Valley J. W. (2010) Crystal orientation effects in $\delta^{18}O$ for magnetite and hematite by SIMS. *Chem. Geol.* **276**, 269–283.

Hung A., Muscat J., Yarovsky I. and Russo S. P. (2002a) Density-functional theory studies of pyrite $FeS_2$ (111) and (210) surfaces. *Surf. Sci.* **520**, 111–119.

Hung A., Muscat J., Yarovsky I. and Russo S. P. (2002b) Density-functional theory studies of pyrite $FeS_2$ (100) and (110) surfaces. *Surf. Sci.* **513**, 511–524.

Hyland M. M. and Bancroft G. M. (1989) An XPS study of gold deposition at low temperatures on sulphide minerals: reducing agents. *Geochim. Cosmochim. Acta* **53**, 367–372.

Killian C. E., Metzler R. A., Gong Y. U. T., Olson I. C., Aizenberg J., Politi Y., Wilt F. H., Scholl A., Young A., Doran A., Kunz M., Tamura N., Coppersmith S. N. and Gilbert P. U. P. A. (2009) Mechanism of calcite co-orientation in the Sea Urchin Tooth. *J. Am. Chem. Soc.* **131**, 18404–18409.

Kresse G. and Furthmuller J. (1996) Efficiency of ab-initio total energy calculations for metals and semiconductors using a plane-wave basis set. *Comput. Mater. Sci.* **6**, 15–50.

Kresse G. and Joubert D. (1999) From ultrasoft pseudopotentials to the projector augmented-wave method. *Phys. Rev. B* **59**, 1758–1775.

Krishnamoorthy A., Herbert F. W., Yip S., Van Vliet K. J. and Yildiz B. (2013) Electronic states of intrinsic surface and bulk vacancies in $FeS_2$. *J. Phys.-Condens. Matter* **25**, 0450411.

Lasaga A. C. (1998) Kinetic Theory in the Earth Sciences, Princeton University Press. Available at: https://www.jstor.org/stable/j.ctt7zvgxm [Accessed March 23, 2019].

Maddox L. M., Bancroft G. M., Scaini M. J. and Lorimer J. W. (1998) Invisible gold: comparison of Au deposition on pyrite and arsenopyrite. *Am. Mineral.* **83**, 1240–1245.

Monkhorst H. J. and Pack J. D. (1976) Special points for brillouin-zone integrations. *Phys. Rev. B* **13**, 5188–5192.

Murowchick J. B. and Barnes H. L. (1987) Effects of temperature and degree of supersaturation on pyrite morphology. *Am. Mineral.* **72**, 1241–1250.

Murphy R. and Strongin D. R. (2009) Surface reactivity of pyrite and related sulfides. *Surf. Sci. Rep.* **64**, 1–45.

Mycroft J. R., Bancroft G. M., Mcintyre N. S. and Lorimer J. W. (1995) Spontaneous deposition of gold on pyrite from solutions containing Au(III) and Au(I) chlorides. 1. A surface study. *Geochim. Cosmochim. Acta* **59**, 3351–3365.

Ohno T., Sarukawa K. and Matsumura M. (2002) Crystal faces of rutile and anatase $TiO_2$ particles and their roles in photocatalytic reactions. *New J. Chem.* **26**, 1167–1170.

Olszta M. J., Cheng X., Jee S. S., Kumar R., Kim Y.-Y., Kaufman M. J., Douglas E. P. and Gower L. B. (2007) Bone structure and formation: a new perspective. *Mater. Sci. Eng.: R: Reports* **58**, 77–116.

Palenik C. S., Utsunomiya S., Reich M., Kesler S. E., Wang L. and Ewing R. C. (2004) "Invisible" gold revealed: direct imaging of gold nanoparticles in a Carlin-type deposit. *Am. Mineral.* **89**, 1359–1366.

Pan J., Liu G., (Max) Lu G. Q. and Cheng H.-M. (2011) On the true photoreactivity order of {001}, {010}, and {101 facets of anatase $TiO_2$ crystals. *Angew. Chem. Int. Ed.* **50**, 2133–2137.

Paquette J. and Reeder R. (1990) New type of compositional zoning in calcite - insights into crystal-growth mechanisms. *Geology* **18**, 1244–1247.

Paquette J. and Reeder R. (1995) Relationship between surface-structure, growth-mechanism, and trace-element incorporation in calcite. *Geochim. Cosmochim. Acta* **59**, 735–749.

Perdew J. P., Burke K. and Ernzerhof M. (1996) Generalized gradient approximation made simple. *Phys. Rev. Lett.* **77**, 3865–3868.

Pshenichkin A. Y., Ananyev Y. S., Bushmano A. I. and Abramova R. N. (2015) Exploration and local forecast of gold-ore deposits based on typomorphic properties of pyrite. *IOP Conf. Ser. Earth Environ. Sci.* **27** 012008.

Rosso K. M. (2001) Structure and reactivity of semiconducting mineral surfaces: convergence of molecular modeling and experiment. *Rev. Mineral. Geochem.* **42**, 199–271.

Rosso K. M., Becker U. and Hochella M. F. (1999) Atomically resolved electronic structure of pyrite {100} surfaces: An experimental and theoretical investigation with implications for reactivity. *Am. Mineral.* **84**, 1535–1548.

Rosso K. M., Becker U. and Hochella M. F. (2000) Surface defects and self-diffusion on pyrite {100}: an ultra-high vacuum scanning tunneling microscopy and theoretical modeling study. *Am. Mineral.* **85**, 1428–1436.

Sazonov A. M., Zvyagina E. A. and Leont'ev S. I. (2009) Typomorphism of pyrite of the gold mineral deposit. *Geochim. Cosmochim. Acta* **73**, A1165.

Schreiner E., Nair N. N. and Marx D. (2008) Influence of extreme thermodynamic conditions and pyrite surfaces on peptide synthesis in aqueous media. *J. Am. Chem. Soc.* **130**, 2768–2770.

Shen J., Li S., Ma G., Liu Y., Yu H. and Liu H. (2013) Typomorphic characteristics of pyrite from the Linglong gold deposit: its vertical variation and prospecting significance. *Earth Sci. Front.* **20**, 55–75.

Sun C. M. and He Z. W. (1997) Characteristics of pyrite from gold deposits in Beishan distinct, Xinjiang. *Acta Pet. Miner.* **16**, 36–39.

Tauson V. L., Kravtsova R. G., Makshakov A. S., Lipko S. V. and Arsentev K. Y. (2017) Contrasting surficial composition of native gold from two different types of gold ore deposits. *Minerals* **7**, 142.

Tauson V. L., Kravtsova R. G., Smagunov N. V., Spiridonov A. M., Grebenshchikova V. I. and Budyak A. E. (2014) Structurally and superficially bound gold in pyrite from deposits of different genetic types. *Russ. Geol. Geophys.* **55**, 273–289.

Tauson V. L., Lipko S. V., Smagunov N. V. and Kravtsova R. G. (2018) Trace element partitioning dualism under mineral-fluid interaction: origin and geochemical significance. *Minerals* **8**, 282.

Teng H. H., Chen Y. and Pauli E. (2006) Direction specific interactions of 1,4-dicarboxylic acid with calcite surfaces. *J. Am. Chem. Soc.* **128**, 14482–14484.

Wang X., Yang X. and Rui H. (2017) The crystal form typomorphism of pyrite and its variation regularity and prospecting significance in Daiwangshan gold deposit, Inner Mongolia. *Gold Sci. Technol.* **25**, 39–46.

Wächtershäuser G. (1992) Groundworks for an evolutionary biochemistry - the iron sulfur world. *Prog. Biophys. Mol. Bio.* **58**, 85–201.

Widler A. M. and Seward T. M. (2002) The adsorption of gold(I) hydrosulphide complexes by iron sulphide surfaces. *Geochim. Cosmochim. Acta* **66**, 383–402.

Xue J., Li S., Sun W., Zhang Y. and Zhang X. (2014) Characteristics of the genetic mineralogy of pyrite and its significance for prospecting in the Denggezhuang gold deposit, Jiaodong Peninsula, China. *Sci. China Earth Sci.* **57**, 644–661.

Yang J.-H. and Zhou X.-H. (2001) Rb-Sr, Sm-Nd, and Pb isotope systematics of pyrite: implications for the age and genesis of lode gold deposits. *Geology* **29**, 711–714.

Yang Z. and Huang M. (1997) Typomorphic peculiarities of pyrites and their application for location prognosis in depth in a gold deposit, Shandong province. *Miner. Resour. Geol.* **11**, 113–118.

Yanina S. V. and Rosso K. M. (2008) Linked reactivity at mineral-water interfaces through bulk crystal conduction. *Science* **320**, 218–222.

Zhang Y. N., Hu J., Law M. and Wu R. Q. (2012) Effect of surface stoichiometry on the band gap of the pyrite $FeS_2$(100) surface. *Phys. Rev. B* **85** 085314.

Zhang Y. N., Law M. and Wu R. Q. (2015) Atomistic modeling of sulfur vacancy diffusion near iron pyrite surfaces. *J. Phys. Chem. C* **119**, 24859–24864.

Zhang Z. and Yates J. T. (2012) Band bending in semiconductors: chemical and physical consequences at surfaces and interfaces. *Chem. Rev.* **112**, 5520–5551.

Zhu J., Xian H., Lin X., Tang H., Du R., Yang Y., Zhu R., Liang X., Wei J., Teng H. H. and He H. (2018) Surface structure-dependent pyrite oxidation in relatively dry and moist air: Implications for the reaction mechanism and sulfur evolution. *Geochim. Cosmochim. Acta* **228**, 259–274.

*Associate editor:* Marc Blanchard